IEEE Access
Multidisciplinary | Rapid Review | Open Access Journal

Received 2 May 2024, accepted 18 May 2024, date of publication 23 May 2024, date of current version 3 June 2024.

Digital Object Identifier 10.1109/ACCESS.2024.3404480

RESEARCH ARTICLE

VO_2-Graphene Ultrathin Films: Enabling Wideband Switchable and Tunable THz Absorption

PATRI UPENDER[1], P. A. HARSHA VARDHINI[2], (Senior Member, IEEE), KRISHNA KUMBA[3], S. PRASANNA BHARATHI[1], AND AMARJIT KUMAR[4], (Senior Member, IEEE)

[1]School of Electronics Engineering, Vellore Institute of Technology, Chennai, Tamil Nadu 600127, India
[2]Department of Electronics and Communication, Vignan Institute of Technology and Science, Hyderabad, Telangana 508284, India
[3]School of Electrical Engineering, Vellore Institute of Technology, Chennai, Tamil Nadu 600127, India
[4]Department of Electronics and Communication, National Institute of Technology Warangal, Hanamkonda, Telangana 506004, India

Corresponding author: Patri Upender (upender.p@vit.ac.in)

This work was supported by Vellore Institute of Technology, Chennai, Tamil Nadu, India.

ABSTRACT This paper presents a groundbreaking advancement in terahertz (THz) technology through the introduction of a novel ultrathin absorber. Composed of vanadium dioxide (VO_2) and graphene, this absorber offers a non-metallic solution for wideband absorption, covering an impressive frequency range from 1.198 THz to 8.752 THz (7.554 THz). Our absorber exhibits exceptional tunable and switchable performance, a significant achievement considering the challenge of achieving frequency tunability across broadband absorption ranges, which was the primary focus of our research endeavor. Furthermore, our proposed absorber demonstrates remarkable characteristics, achieving up to 80% absorption even at high incidence angles of up to 80°. Additionally, the absorber enhances Shielding Effectiveness in electromagnetic interference (EMI) shields and stealth systems, further highlighting its versatility and potential impact in various applications.

INDEX TERMS Absorber, graphene, switchable, tunable, VO_2, wideband.

I. INTRODUCTION

Terahertz (THz) frequency, occupies a unique electromagnetic (EM) spectrum characterized by its potential for diverse applications across various fields [1], [2], [3]. The THz region, often referred to as the ''THz gap,'' bridges the gap between the microwave and infrared regimes, offering a wealth of opportunities for exploration and innovation. Moreover, THz technology has emerged as a promising frontier in science and engineering, propelled by its ability to penetrate a wide range of materials, including clothing, plastics, paper, and biological tissues, while also exhibiting low photon energy, non-ionizing radiation, and high spectral resolution [4], [5]. In addition, in recent years, research efforts in THz technology have surged, driven by the quest to unlock its vast potential. Furthermore, scientists and engineers have developed a myriad of devices tailored to exploit the unique properties of THz radiation. These devices encompass a diverse range of applications, including communication systems, imaging techniques, spectroscopy, medical diagnostics, security screening, and sensing technologies [6], [7]. Among the various devices designed for operation within the THz frequency region, absorbers play a particularly crucial role. Absorbers, also known as absorptive materials or absorptive coatings, are engineered structures that efficiently capture and dissipate incident THz radiation. Moreover, in addition to traditional absorbers, Metamaterials (MM) have emerged as a transformative technology in the realm of THz frequency applications [8], [9], [10]. MM are engineered structures with properties not found in naturally occurring materials, offering unprecedented control over EM waves at THz frequencies. While metallic absorbers have traditionally dominated the field of THz absorption, non-metallic absorbers, particularly those based on materials like Vanadium dioxide (VO_2),

The associate editor coordinating the review of this manuscript and approving it for publication was Saroj Tripathi.

have garnered increasing attention due to their unique properties and advantages. Non-metallic absorbers offer distinct advantages over metallic counterparts, including lower losses, dynamic tunability, and compatibility with integrated circuit fabrication processes [11], [12]. VO_2, in particular, undergoes a phase transition from an insulating to a metallic state at a critical temperature, enabling reversible modulation of its electrical and optical properties. This phase transition behavior makes VO_2-based absorbers highly versatile and suitable for a wide range of THz applications, including dynamic switching devices, adaptive camouflage systems, and temperature-sensitive sensors [13], [14], [15], [16]. Graphene-based absorbers also hold promise, with graphene's unique properties enabling efficient THz absorption and tunability [17], [18]. The fusion of graphene and VO_2 offers unparalleled tunability, with dynamic adaptation enabled by VO_2's phase transition and enhanced functionality, including durability, flexibility, and compatibility with emerging THz technologies. This versatility positions the absorber as a cornerstone in the next generation of THz devices.

Several studies have investigated the development of THz MM based VO_2 absorbers, each offering unique design features and promising applications. In [19], a VO_2-based absorber for CO_2 gas sensing integrates a MM perfect absorber with a MEMS-based microheater, enabling switchable optical properties with high absorption efficiency and rapid response. Yet, fabrication complexity and the requirement for precise temperature and voltage control pose challenges. Moreover in [20], an active broadband perfect absorber MM based on hexagonal-patterned VO_2 is proposed, achieving adjustable absorption within the 6.5 to 7.90 THz range. Yet, it exhibits a low modulation depth and requires a high operating temperature. In [21], researchers explore a tunable broadband THz MM absorber utilizing VO_2, achieving over 90% absorption with a 0.33 THz bandwidth but falling short of practical expectations. Additionally, [22] discusses dynamic and polarization-insensitive MM based on VO_2. However, MM perfect absorbers with metal/insulator/metal structures face limitations, hindering practical use. Furthermore, [23] explores a tunable broadband THz MM absorber using VO_2, suffering from structural complexity. Moreover, [24] illustrates the transition to ultra-wideband THz MM absorbers, showcasing a perfect absorber achieving over 99% absorption in the 6.6-8.9 THz range. In [25], a VO_2-based absorber with a multi-ring structure achieves dynamic absorption control via VO_2's phase-change properties sensitive to temperature. However, its complex structure may pose fabrication challenges. The authors in [14], a THz absorber design employs graphene and VO_2 for multi-channel control, promising diverse applications but facing fabrication complexities. Additionally, the absorber in [26] achieves over 90% perfect absorption within the 3.01–6.79 THz range, utilizing graphene and VO_2 properties for dynamic absorption control, despite design complexity. In the pursuit of addressing the evolving demands of modern technology, there arises a clear imperative for the development of absorber that are not only simple and compact but also nonmetallic, tunable and switchable, capable of offering wide-ranging absorption properties.

In this paper, we introduce a novel ultrathin absorber composed of VO_2 and graphene, offering a non-metallic solution for wideband absorption spanning from 1.198 THz to 8.752 THz (7.554 THz). This absorber demonstrates remarkable tunable and switchable performance, a challenging feat in achieving frequency tunability across broadband absorption ranges, which constitutes the primary focus of our research endeavor. Moreover, our proposed absorber showcases outstanding characteristics, boasting up to 80% absorption even at high incidence angles of up to 80°. The proposed absorber also contributes to enhancing Shielding Effectiveness in EM interference (EMI) shields and stealth systems. Three scenarios are explored: varying the graphene chemical potential (μ_c) from 0.1 eV to 0.9 eV while maintaining VO_2 in the insulating phase (Case i), altering the conductivity of VO_2 (σ_{VO_2}) while keeping μc constant at 0 eV (Case ii), and varying the μ_c from 0.1 eV to 0.9 eV while maintaining VO_2 in the conducting phase (Case iii). Exploring these cases is crucial for understanding the fundamental mechanisms underlying the tunable and switchable properties of the proposed absorber.

II. DESIGN OF THE PROPOSED ABSORBER

Fig. 1 illustrates the structure of the proposed absorber. Fig. 1(a) details the periodic pattern and unit cell configuration, illustrating the interface of incoming EM waves with the absorber. The absorber comprises a bottom silicon dioxide (SiO_2) substrate with a relative permittivity of $\varepsilon_s = 2.2$ and a loss tangent ($tan\ \delta$) of 0.006. The periodicity (L×W) is set at 80 × 80 μm, and the substrate thickness is denoted as t_s. A graphene layer, grown atop the SiO_2 layer with a thickness of t_g, is characterized by an initial $\mu_c = 0.1$ eV at T = 300 K and a relaxation time (τ) of $\tau = 0.1$ ps. Graphene is a 2D material composed of a single layer of carbon atoms arranged in a hexagonal lattice. The electrical and optical properties of graphene can be tuned by adjusting its μ_c. This tunability provides flexibility in tailoring the absorber's performance to specific frequency. The surface conductivity (σ_G) of graphene is given by the sum of intraband (σ_{intra}) and interband (σ_{inter}) conductivity terms are determined using the Kubo formula [27], [28], [29], [30] which are expressed by equations (1)-(3):

$$\sigma_G(\omega, \tau, \mu_c, T) = \sigma_{intra}(\omega, \tau, \mu_c, T) + \sigma_{inter}(\omega, \tau, \mu_c, T) \tag{1}$$

$$\sigma_{intra}(\omega, \tau, \mu_c, T) \approx -j\frac{e^2 k_B T}{\pi\hbar^2\left(\omega - j\tau^{-1}\right)} \times \left[\frac{\mu_c}{k_B T} + 2ln\left[exp\left(-\frac{\mu_c}{k_B T}\right) + 1\right]\right] \tag{2}$$

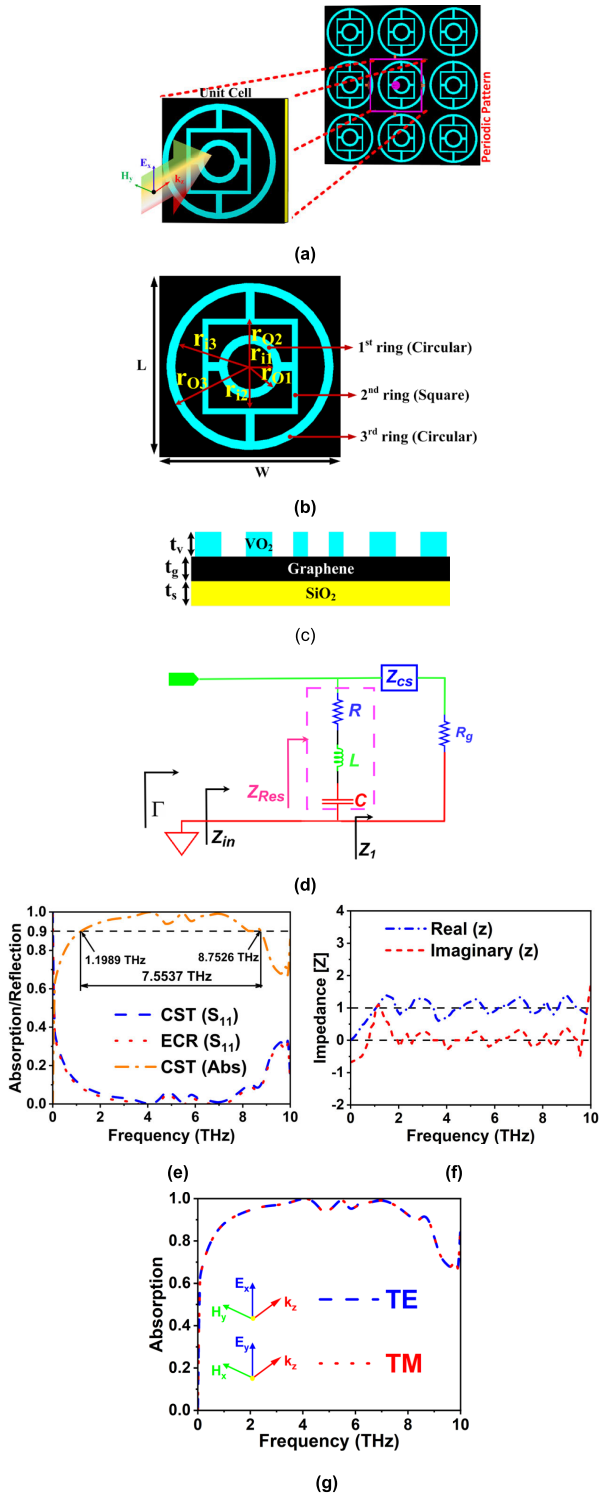

FIGURE 1. Proposed absorber (a) Unit cell and periodic pattern, (b) Unit cell with dimensions, (c) Front view, (d) CS, (e) Absorption and reflection coefficient, (f) Impedance (Z), and (g) TE and TM modes. ($R = 2\times10^{-6}\Omega, L = 3.18nH, C = 3.19fF$).

$$\sigma_{inter}(\omega, \tau, \mu_c, T) \approx -j\frac{e^2}{4\pi\hbar} ln\left[\frac{2|\mu_c| + (\omega - j\tau^{-1})\hbar}{2|\mu_c| - (\omega - j\tau^{-1})\hbar}\right] \quad (3)$$

where charge of the electron (e), Boltzmann constant (k_B), Planck constant ($\hbar$) [29], [30], [31]. In simulations, the graphene layer is represented as a thin layer with a thickness of $t_g = 0.34$ nm, characterized by a complex permittivity $\varepsilon_g = \varepsilon_0 - j(\sigma_g(\omega)/t_g\omega)$, where σ_g is the conductivity of graphene. The conductivity of graphene can be adjusted by modulating the chemical potential of the graphene. The chemical potential can be varied in CST Microwave Studio.

On the graphene layer, three rings made of VO_2 are positioned. VO_2 is a compound that undergoes a phase transition at a specific critical temperature. Below this temperature, VO_2 is in the insulating phase, while above it, it transitions to the metallic phase. Furthermore, with a temperature increase from 300 to 360K, the VO_2 material transitions from its insulating phase to a conducting phase, resulting in a variation in conductivity from $1 \times 10^2 S/m$ to $5\times10^5 S/m$, respectively. The versatility of VO_2 in transitioning between insulating and metallic phases has catalyzed the development of switchable devices. The VO_2 layer is modeled as a layer with a thickness of t_v, and its relative permittivity is defined accordingly. The permittivity of VO_2 is dependent on its thermal excitation. The permittivity of VO_2, both its real and imaginary components, are given by equations (4)-(6) [32], [33], [34].

$$\varepsilon_{VO_2} = \frac{1}{4}\left\{\varepsilon_d(2-3V) + \varepsilon_m(3V-1) + \sqrt{\varepsilon_d(2-3V) + \varepsilon_m(3V-1)^2 + \varepsilon_d\varepsilon_m}\right\} \quad (4)$$

The relative permittivity of VO_2 can be described through Drude model.

$$\varepsilon(\omega) = \varepsilon_\infty - \frac{\omega_p^2(\sigma)}{\omega(\omega + i\gamma)} \quad (5)$$

where $\varepsilon_\infty = 12$ is the permittivity at the infinite frequency. $\omega_p(\sigma_0)$ is calculated using equation 6.

$$\omega_p^2(\sigma_{VO_2}) = (\sigma_{VO_2}/\sigma_0)\,\omega_p^2(\sigma_0) \quad (6)$$

The plasma frequency, denoted as $\omega_p(\sigma_0) = 1.4 \times 10^{15}$ rad/s and $\gamma = 5.75 \times 10^{13}$ rad/s represents the damping rate parameter.

The three VO_2 rings that are placed on the graphene layer include (i) the 1st ring in a circular shape with radii of r_{i1}, and r_{O1}, respectively (ii) the 2nd ring in a square shape, with radii of r_{i2}, and r_{O2}, respectively and (iii) the 3rd ring in a circular ring shape with radii of r_{i3}, and r_{O3}, respectively. The dimensions of these rings and the layers are presented in Fig. 1(b) and Fig. 1(c). The arrangement of VO_2 rings during the metallic phase provides a wideband absorption bandwidth ranging from 1.198 THz to 8.752 THz (7.554 THz) with a centre frequency (f_c) of 4.975 THz. The circuit schematic (CS) of the suggested absorber is illustrated in Fig. 1(d). The absorber's high absorption is attributed to EM resonances occurring within its structure, thereby defining its functionality through the CS.

The absorber configuration is devoid of metal, with the resistive characteristic facilitated by the VO_2 resonators and graphene reflector. The VO_2 material contribute to its dispersive properties, resulting in effective impedance and functioning as the medium. This medium is terminated at the dispersive graphene reflector, providing resistance R_g. The impedance offered by the VO_2 layer is expressed as $Z_{CS} = Z_{VO_2} = \eta_0 / \sqrt{\epsilon}_{VO_2}$, where η_0 represents free-space impedance.

The impedance at the transmission line's input terminal can be computed using the following equation (7).

$$Z_1 = Z_{CS} \left[\frac{R_g + jZ_{CS} \tan \beta t_v}{Z_{CS} + jR_g \tan \beta t_v} \right] \tag{7}$$

The resonance exhibited by the absorber structure can be illustrated using the series RLC circuit, which provides a bandpass response. In this context, the resistance value can be determined utilizing the conductivity of the VO_2 resonator as $R \approx 1/\sigma_{VO_2}$. The inductance and capacitance values can be computed at the resonance frequency, taking into account the center frequency of the operational bandwidth. The impedance offered by the resonance circuit is denoted as Z_{Res}, and the total input impedance can be calculated as $Z_{in} = Z_{Res} \parallel Z_1$. Utilizing the calculated input impedance, the reflection coefficient is estimated using the following equation, assuming zero imaginary part. The reflection coefficient is subsequently computed with $\Gamma = (Z_{in} - \eta_0) / (Z_{in} + \eta_0)$, considering the zero-imaginary part of the Z_{in}. The agreement between simulated and calculated results confirms the validity of the absorber's operation. The absorption and reflection plots of CS, and CST are shown in fig. 1(e). The absorption coefficient (A) is calculated using equations 8 and 9.

$$A = 1 - R - T = 1 - \left(\frac{Z_{eff} - Z_0}{Z_{eff} + Z_0} \right) = 1 - \left(\frac{Z_{rel} - Z_0}{Z_{rel} + Z_0} \right)^2 \tag{8}$$

$$Z_{rel} = \sqrt{\frac{(1 + S_{11})^2 - S_{21}^2}{(1 - S_{11})^2 - S_{21}^2}} \tag{9}$$

Here R is the reflection coefficient, given by $R = |S_{11}^2|$, and T is the transmission coefficient, given by $T = |S_{21}^2|$. The graphene layer at the bottom having a thickness of 0.34 nm, provides the perfect reflection making $T = 0$. The relation between A, effective impedance (Z_{eff}), relative impedance (Z_{rel}) and free space impedance (Z_0) is given in equation 8.

The real and imaginary parts of the impedance plots are shown in Fig. 1(f). The observations indicate that the real part of the impedance approximates unity, while the imaginary part approaches zero across the frequency spectrum, implying a close alignment between the absorber's impedance and the characteristic impedance of free space. Consequently, no reflections occur, leading to the achievement of perfect absorption. In Figure 1(g), the absorption characteristics of the proposed absorber are presented under both TE and TM incidences. The uniform response observed for both incidences suggest the structural symmetry of the absorber.

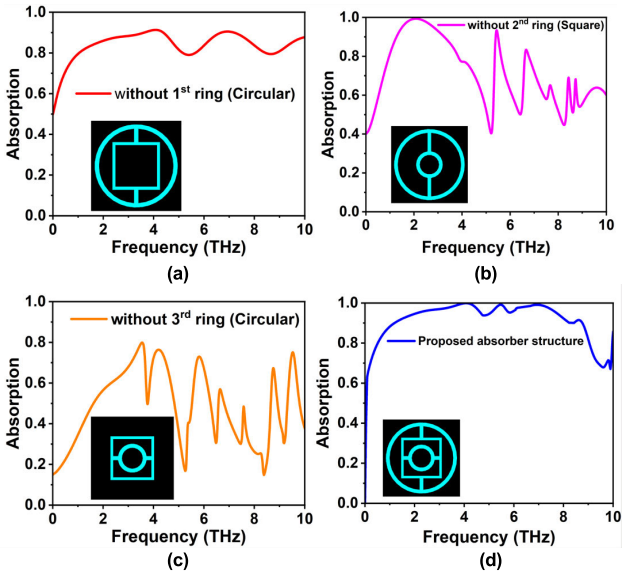

FIGURE 2. Absorption plots for different configurations of (a) Configuration-I, (b) Configuration-II, (c) Configuration-III, and (d) Proposed configuration.

III. EVOLUTION OF THE PROPOSED ABSORBER

Fig. 2 illustrates the absorption plots for various absorber structures achieved by removing different rings from the proposed absorber. In the first absorber structure depicted in Fig. 2(a), the circular-shaped 1st ring is removed. The absorption spectra exhibit consistent high absorption rates exceeding 80% across the entire frequency band. The reduction in absorption can be attributed to the absence of the 1st ring. Fig. 2(b) presents the absorption spectra plot after removing the 2nd ring, which is square-shaped. The absorber demonstrates a multiband behavior, indicating absorption across multiple frequency bands. The absence of the 2nd ring results in a narrower absorption bandwidth, suggesting that the 2nd ring significantly contributes to achieving wideband absorption in the absorber structure.

In Fig. 2(c), the gradual decrease in absorption rate is observed when removing the 3rd ring, which has a circular shape. This behavior is depicted in the absorption spectra. The reduction in absorption can be attributed to the strong absorption characteristics of the 3rd ring. The accumulation of charge carriers is diminished in the absence of this ring, resulting in a lower absorption rate for this modified structure. In the proposed absorber structure depicted in Fig. 2(d), where all the rings are present, the absorber demonstrates robust charge accumulation. It exhibits a wideband response ranging from 1.198 THz to 8.752 THz with absorptivity of $>90\%$, with an observed percentage bandwidth of 151.83%.

IV. PERFORMANCE ANALYSIS

The performance of the proposed absorber is investigated by varying its physical parameters, including the radius of

the 1st ring (r_{o1}, r_{i1}), 2nd ring (r_{o2}, r_{i2}), 3rd ring (r_{o3}, r_{i3}), thickness of the VO_2 layer (t_v), and thickness of SiO_2 (t_s). Absorption spectra along with electric field (EF) distribution (EFD) for these parameters is investigated to understand their influence on the absorber's performance. Only one parameter is changed by keeping other parameters intact. In the first set, the outer ring radius (ro1) of the 1st ring is systematically varied from 12 to 16 μm with a period change of 1 μm, as illustrated in Fig. 3(a). For lower values of ro1, the absorber exhibits lower absorption, approximately 85%. This may be attributed to reduced interaction between incident EM waves and the absorber structure, as evidenced by the EF distribution shown in Fig. 3(a). When $r_{o1} = 14$ μm, the absorber shows improved absorption, likely due to enhanced resonance and increased interaction, resulting in better overall performance. However, for higher values of r_{o1}, absorption slightly reduces, as indicated by the EF distribution, which shows less distribution on the VO_2 rings. The reason for less absorption for higher values of r_{o1} can be attributed to the reduced interaction between incident EM waves and the absorber structure. As the r_{o1} increases, there is a decrease in the effective coupling between the incident waves and the absorber, leading to a decline in the absorption efficiency. Additionally, at higher values of r_{o1}, the distribution of the EF tends to concentrate less on the VO_2 rings, resulting in decreased absorption.

In the subsequent analysis, the inner radius (r_{i1}) of the 1st ring is systematically adjusted from 8 μm to 12 μm with a period change of 1 μm as illustrated in Fig. 3(b). The absorber exhibits a slightly lower absorption percentage, below 90%, for smaller values of r_{i1}. However, at $r_{i1} = 10$ μm, the absorber demonstrates excellent absorption with wideband characteristics. The observed variations in absorption can be attributed to the impact of changing r_{i1} on the resonant behavior and interaction of the absorber with incident EM waves. Moreover, the EFD analysis reveals that for higher values of r_{i1}, there is a reduction in absorption efficiency. This reduction can be attributed to the distribution of the EF, which shows less concentration on the VO_2 rings as r_{i1} increases, thus resulting in decreased absorption.

Continuing with the analysis, the outer radius of the 2nd ring (r_{o2}) is systematically changed from 28 μm to 32 μm with an increment of 1 μm as shown in Fig. 3(c). Lower values of r_{o2} result in an absorption percentage ranging between 80% to 85%. However, at $r_{o2} = 30$ μm, the absorber exhibits excellent absorption characteristics and demonstrates wideband absorption performance. The observed trend suggests that adjusting r_{o2} influences the absorber's resonant behavior and its ability to interact effectively with incident EM waves, affecting the overall absorption performance. Moreover, the EFD analysis reveals that for $r_{o2} = 30$ μm, the EF is more concentrated around the VO_2 rings, indicating enhanced interaction and absorption efficiency. For higher r_{o2} values, absorption slightly decreases due to the altered distribution of the EF, leading to reduced interaction with the VO_2 rings. For higher r_{i2} values, absorption slightly decreases due to the altered distribution of the EF, leading to reduced interaction with the absorber structure, resulting in a slight reduction in absorption efficiency.

Moving forward, the inner radius of the 2nd ring (r_{i2}) is systematically changed from 24 μm to 28 μm with an increment of 1 μm. Lower values of r_{i2} result in absorption below 80%. However, at $r_{i2} = 26$ μm, the absorber demonstrates a wideband absorption bandwidth, providing over 90% absorption, as depicted in Fig. 3(d). This suggests that the adjustment of r_{i2} significantly influences the absorber's resonant characteristics and its ability to achieve higher absorption rates across a broader frequency range. For higher r_{i2} values, absorption slightly decreases due to the altered distribution of the EF, leading to reduced interaction with the absorber structure, resulting in a slight reduction in absorption efficiency.

Fig. 3(e) and Fig. 3(f) depict the absorption spectra for the variation of the outer and inner radius of the 3rd ring (r_{o3}, r_{i3}), respectively. When r_{o3} is set to 30 μm and r_{i3} to 33 μm, the absorber exhibits wideband absorption spectra with an absorption bandwidth of 151.83%. This suggests that adjusting the outer and inner radii of the 3rd ring plays a crucial role in achieving enhanced absorption performance across a broad frequency range. For higher values of r_{o3} and r_{i3}, the decrease in absorption can be attributed to the altered distribution of the EF. This alteration results in reduced interaction between incident EM waves and the absorber structure, leading to a slight decrease in absorption efficiency.

In Fig. 3(g), the absorption spectra are depicted for the change in the thickness of the VO_2 film (t_v) from 0.05 μm to 0.15 μm at an increment of 0.025 μm. The absorber exhibits wideband absorption spectra for $t_v = 0.1$ μm. However, for higher or lower values of t_v, the absorber performance gradually changes and does not provide wideband absorption characteristics. The decrease in absorption for higher or lower values of tv can be attributed to the altered thickness of the VO_2 film. At the optimal thickness of $t_v = 0.1$ μm, the absorber demonstrates wideband absorption spectra. However, deviations from this thickness result in changes to the resonant behavior and interaction of the absorber with incident EM waves, leading to reduced absorption efficiency and the loss of wideband absorption characteristics.

Finally, Fig. 3(h) illustrates the absorption spectra with variations in the SiO_2 layer thickness (t_s) from $t_s = 0.3$ μm to $t_s = 0.7$ μm. At $t_s = 0.5$ μm, the absorber demonstrates excellent absorption characteristics. Deviating from this value, either by increase or decrease, results in a deterioration of the absorber's performance. The decrease in absorption, when deviating from the optimal SiO_2 layer thickness ($t_s = 0.5$ μm), is attributed to changes in the interaction with incident waves. At the optimal thickness, enhanced resonance leads to excellent absorption, as indicated by EF distribution. Deviations disrupt this resonance, reducing absorption efficiency. Therefore, optimizing both VO_2 and SiO_2 layer thickness is crucial for wideband absorption. This indicates that the optimization of the thickness of the VO_2

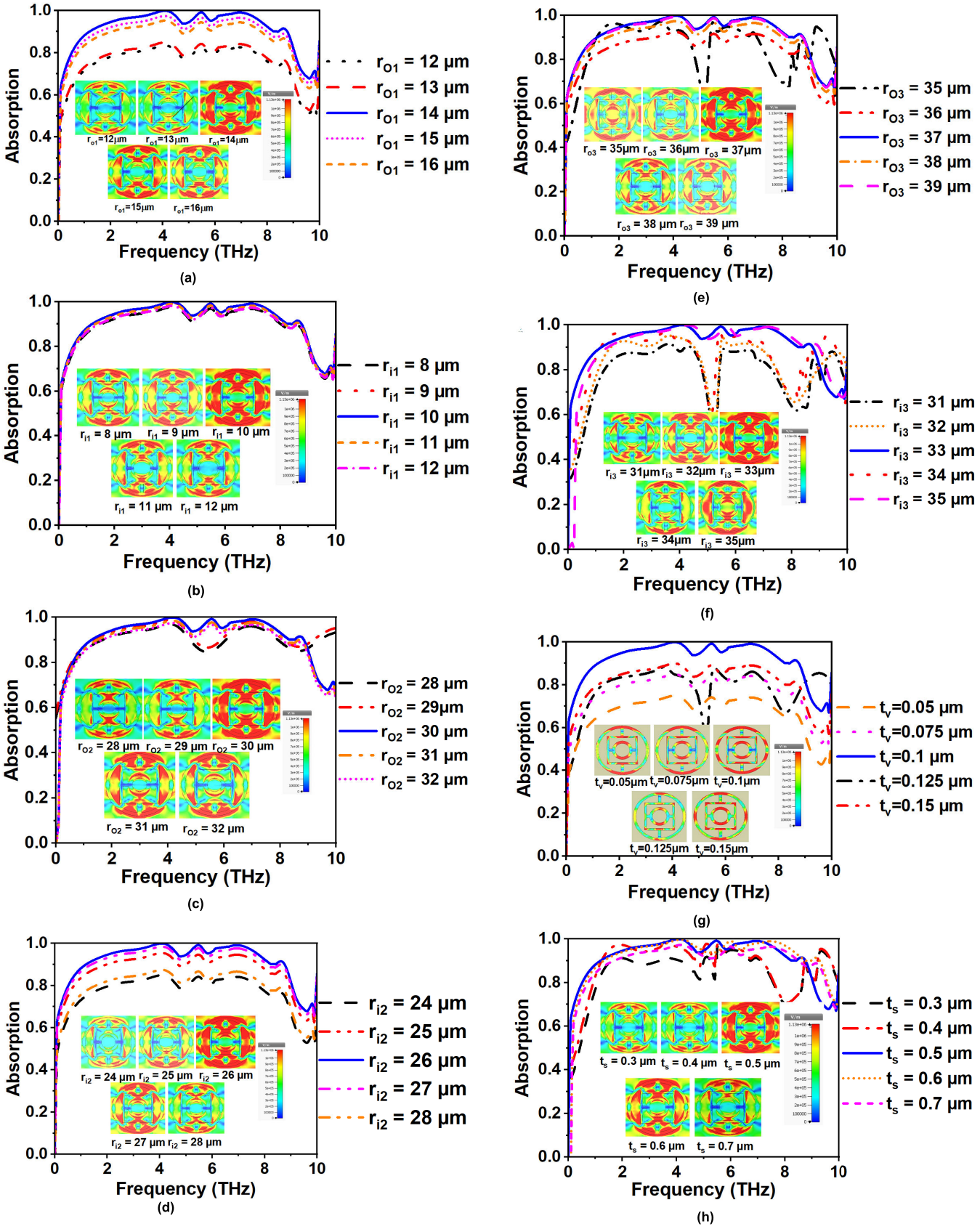

FIGURE 3. Absorption spectra and EF distribution for change in (a) r_{O1}, (b) r_{i1}, (c) r_{O2}, (d) r_{i2}, (e) r_{O3}, (f) r_{i3}, (g) t_v, and (h) t_s.

and SiO_2 layers is crucial for achieving the desired wideband absorption characteristics in the absorber structure.

In conclusion, the systematic analysis of the proposed absorber structure's performance by varying key physical parameters, including outer and inner radii of the 1st, 2nd, and 3rd rings (r_{o1}, r_{i1}, r_{o2}, r_{i2}, r_{o3}, r_{i3}), as well as the thickness of the VO_2 layer (t_v) and the SiO_2 layer (t_s), has provided valuable insights. Optimal adjustments of these parameters have been identified to enhance the absorber's absorption characteristics. Specifically, the absorber exhibits excellent performance when the outer radius of the 1st ring (r_{o1}) is set to 14 μm, the inner radius of the 2nd ring (r_{i2}) is 26 μm, and both the outer (r_{o3}) and inner (r_{i3}) radii of the 3rd ring are set to 30 μm and 33 μm, respectively. Additionally, a VO_2 layer thickness (t_v) of 0.1 μm and a SiO_2 layer thickness (t_s) of 0.5 μm contribute to achieving wideband absorption characteristics. These findings underscore the importance of carefully tuning these parameters for optimizing the absorber's performance in diverse applications.

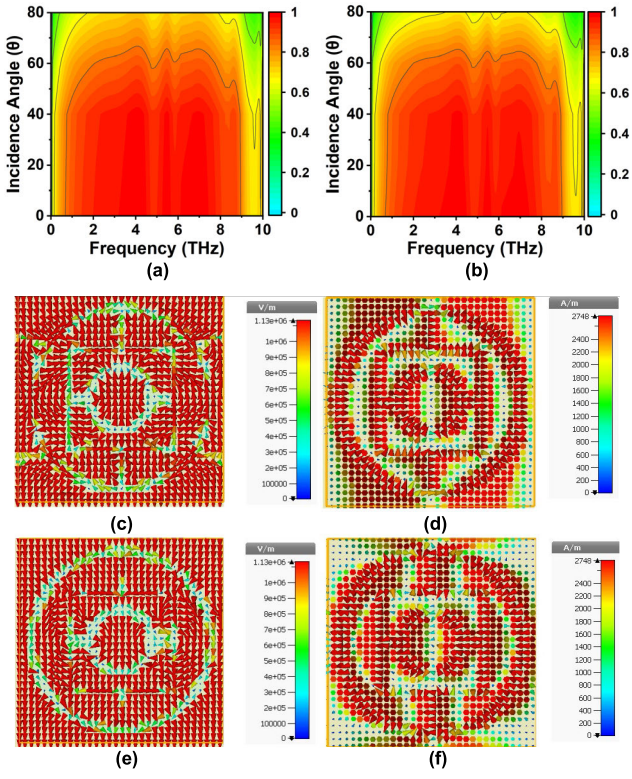

FIGURE 4. Absorption performance at various incidence angles under (a) TE, and (b) TM polarizations. (c), (d) EF and H under TE incidence. (e), (f) EF and H under TM incidence.

V. TE AND TM INCIDENCE

Fig. 4 depicts the absorption plots of proposed absorber for various incidence angles (θ) ranging from 0° to 80° under TE and TM incidence. Under TE (Transverse magnetic) incidence, as illustrated in Fig. 4(a), the suggested absorber achieves absorption rates exceeding 80% for angles $\theta < 75°$. Particularly noteworthy is its excellent absorption, surpassing 90%, for angles $\theta < 60°$ within the operating frequency band spanning from 1.198 THz to 8.752 THz. However, as the $\theta > 75°$, the absorption diminishes. As the incidence angle becomes steeper, the efficiency of interaction between the incident waves and the absorber will decrease. This reduced interaction will result in less effective absorption and, consequently, lower absorptivity at higher incidence angles ($\theta < 80°$). Under TM (Transverse magnetic) occurance, as shown in Fig. 4(b), the recommended absorber exhibits excellent absorption characteristics. For $\theta < 75°$, the absorber demonstrates absorption rates exceeding 90% and gradually decreases as the incidence angle increases. In the range between 55° and 75°, the absorber maintains absorption levels above 80%, but performance starts to deteriorate beyond 75°. This behavior suggests that the absorber is particularly effective for TM-polarized incident waves at lower incidence angles, making it appropriate for applications such as THz imaging, sensing, and communication systems operating within the specified angular range. The absorber's performance under different polarization conditions enhances its versatility for various THz applications.

Fig. 4(c) – Fig 4(f) displays the EM field distribution of our proposed structure under TE and TM polarizations. The three VO_2 rings drive absorption, supported by the graphene sheet. Under TE polarization, the EF intensity peaks show high concentration of field vectors around the VO_2 rings, while the magnetic field (H) shows good field distribution around the rings. For TM polarization, EF and H peaks occur around the VO_2 rings. The EFD predominates around the VO_2 rings, while the H distribution is slightly diminished in comparison. Furthermore, due to the shallower absorption depth under TM polarization relative to TE polarization, the EM field distribution under TM polarization is not as prominent as under TE polarization. This underscores, the proposed structure primarily relies on electric resonance for absorption, wherein EM waves interact with the EF components, maximizing absorption efficiency.

Fig. 5(a) depicts the biasing of the proposed absorber. The electrical conductivity of graphene undergoes modification when a direct current (DC) voltage is applied, as referenced to the polysilicon layer. Consequently, this adjustment influences the response of the absorber. As depicted in the Fig. 5(b), we observe that as the bias voltage (V_g) increases from 0 to 3V, the μ_c of graphene also increases from 0 to 1eV for the proposed absorber. This increase in bias voltage leads to a corresponding increase in the conductivity of graphene, resulting in reconfigurable characteristics within the device.

Three scenarios are explored in this investigation: Case (i) involves varying the graphene μ_c from 0.1 eV to 0.9 eV while maintaining VO_2 in the insulating phase. In Case (ii), the conductivity of VO_2 (σ_{VO_2}) is altered while keeping μ_c constant at 0.1 eV. Case (iii) involves varying the μ_c from 0.1 eV to 0.9 eV while maintaining VO_2 in the conducting phase. In Case (i), under the insulating phase of VO_2, an increase in μ_c from 0.1 eV to 0.9 eV results in an augmentation of absorption. At $\mu_c = 0.9$ eV, the absorber

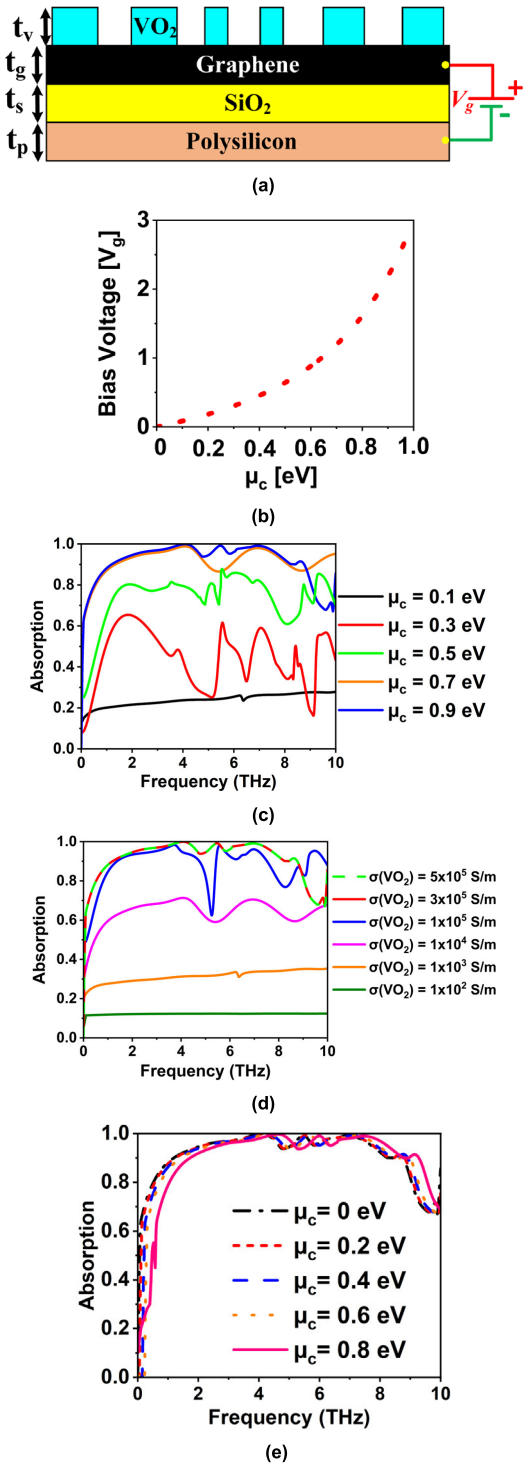

FIGURE 5. (a) Proposed absorber biasing scheme, (b) Bias voltage vs μ_c. Absorber performance for (c) various μ_c values when VO_2 is in an insulating phase ($\sigma_{VO_2} = 1 \times 10^2$ S/m) and (d) various σ_{VO_2} values when $\mu_c = 0.1$ eV, and (e) various μ_c values when VO_2 is in conducting phase.

displays wideband absorption, as depicted in Fig. 5(c). Conversely, as μ_c decreases, there is a corresponding reduction in absorption. At $\mu_c = 0.3$ eV, the absorber resonates in multiple bands with a maximum absorptivity of 60%. At $\mu_c = 0.5$ eV, a maximum absorptivity of 80% is observed, and at $\mu_c = 0.7$ eV, a maximum absorption of 90% is achieved. The increase in μc under the insulating phase of VO_2 leads to an increase in absorptivity due to the tunable nature of graphene's electronic properties.

In the insulating phase of VO_2, it exhibits poor electrical conductivity, limiting its ability to interact with and absorb EM waves effectively. However, introducing graphene with a higher μ_c enhances its conductivity. The increased carrier concentration in graphene enhances its ability to more efficient coupling with incident EM waves. This enhanced coupling results in a higher absorptivity, as a greater portion of the incident energy is absorbed by the absorber. Consequently, graphene becomes highly conductive, allowing it to absorb a broad range of frequencies ranging from 1.198 THz to 8.752 THz. This leads to wideband absorption capabilities of the absorber under the insulating phase of VO_2. In Case (ii), the conductivity of VO_2 (σ_{VO2}) is increased from $\sigma_{VO2} = 1 \times 10^2 S/m$ to $\sigma_{VO2} = 5 \times 10^5 S/m$ while keeping μ_c constant at 0 eV. With increase in σ_{VO2} it is observed that the absorption increases providing wideband absorption $> 90\%$ ranging from 1.198 THz to 8.752 THz for $\sigma_{VO2} = 3 \times 10^5 S/m$ and $\sigma_{VO2} = 3 \times 10^5 S/m$ as depicted in Fig. 5(d). When $\sigma_{VO2} = 1 \times 10^2 S/m$, the absorber shows very less absorption of around 10%. Next, for $\sigma_{VO2} = 1 \times 10^4 S/m$, the absorption increases providing maximum absorption of $> 60\%$. For $\sigma_{VO2} = 1 \times 10^5 S/m$, maximum absorption up to 90% is exhibited. As σ_{VO2} increases, the electrical conductivity of VO_2 improves. Higher σ_{VO2} facilitates better interaction with incident EM waves. At $\mu_c = 0$ eV, graphene itself has limited conductivity. The increased conductivity in VO_2 provides additional pathways for electron flow and enhances the interaction between graphene, VO_2 and incident waves. VO_2 acts as a critical component that amplifies the absorber's capability to interact with and absorb incident EM waves. The improved electrical conductivity in VO_2 provides additional pathways for electron flow, promoting better synergy with the graphene layer. In Case (iii), the absorption characteristics are analyzed across varying values of μ_c while maintaining σ_{VO_2} in the conducting phase as depicted in Fig. 5(e). It is noted that an increase in μ_c corresponds to a frequency shift towards higher frequencies. This observation stems from the role of μ_c in tuning the resonant frequency of the absorber, indicating its influence on the absorption behavior. These scenarios demonstrate the versatility of the absorber's tunable properties and highlight the collaborative impact of both graphene and VO_2 in achieving optimized absorption characteristics for diverse THz applications, ranging from communication devices to sensing and security systems.

VI. FIELD DISTRIBUTION

Fig. 6(a), Fig. 6(b), and Fig. 6(c) shows the Electric Field (EF), Magnetic Field (H), and Surface Current (SC) distribution on the proposed absorber under the condition where the μc is held constant at 0 eV, and different values of σ_{VO_2} are considered. As the σ_{VO_2} increases, a significant

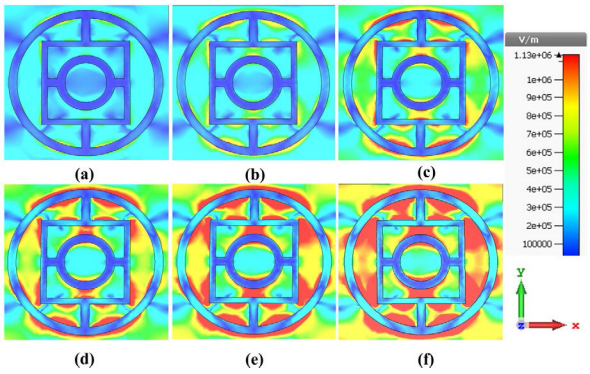

FIGURE 6. EF distribution on the proposed absorber at a frequency of 4.97 THz for different values of conductivity (σ_{VO_2}) in S/m. (a) $\sigma_{VO_2} = 1\times10^2$, (b) $\sigma_{VO_2} = 1\times10^3$, (c) $\sigma_{VO_2} = 1\times10^4$, (d) $\sigma_{VO_2} = 1\times10^5$, (e) $\sigma_{VO_2} = 3\times10^5$, (f) $\sigma_{VO_2} = 5\times10^5$.

rise in charge accumulation is observed, leading to a more pronounced and robust field distribution surrounding the absorber. Initially, when the $\sigma_{VO_2}$is 1×10^2 S/m, both absorption and charge accumulation are very minimal. As the conductivity increases to 1×10^3 S/m, there is a slight increase in charge accumulation on the 3rd ring, resulting in the absorber beginning to absorb incident EM waves.

Further increasing the conductivity to 1×10^4 S/m leads to a notable increase in charge accumulation on the 3rd and 2nd rings, thereby enhancing absorption. With a conductivity of 1×10^5 S/m, there is an increase in charge accumulation on the 3rd, 2nd, and 1st rings, resulting in further absorption enhancement. Similarly, when the conductivity is increased to 3×10^5 and 5×10^5 S/m, there is a considerable increase in charge accumulation across all rings, further augmenting absorption. This augmented distribution significantly contributes to increased absorption efficiency, rendering the absorber more proficient in absorbing incident EM waves. The increase in conductivity results in a higher concentration of charge carriers within the material, which enhances the ability of the absorber to accumulate charge on its rings. When the σ_{VO_2} increases, more charge carriers become available, leading to greater charge accumulation on the rings of the absorber. This phenomenon occurs because the higher conductivity facilitates more efficient movement of charge carriers within the material, allowing them to redistribute and accumulate on the rings of the absorber more effectively. As a result, the charge distribution on the rings increases with the increase in conductivity. It is evident that VO_2 undergoes a phase transition from an insulating state for lower values of $\sigma_{VO_2}$to a conducting state for higher values of σ_{VO_2}. This transition is accompanied by a significant increase in charge accumulation within the VO_2 material, facilitating the absorption of incident EM waves. Therefore, the proposed absorber offers the switching property from the insulating phase to the conducting phase. Moreover, VO_2 serves as a crucial component in switchable devices, enabling the controlled modulation of electrical conductivity. This capability renders VO_2-based devices invaluable in various sectors, including smart windows, thermal regulation systems, and energy-efficient electronics. Additionally, the tunable nature of VO_2 makes it well-suited for THz technologies, enabling the optimization of absorption characteristics and enhanced performance in communication devices, sensing technologies, and security systems across diverse applications.

VII. PROPOSED ABSORBER AS THZ EM SHIELDING

A metal-free, ultrathin configuration enhances shield efficiency, aligning with the need for optimal shielding. This broadband absorber, offering flawless absorption, meets these criteria, making it suitable for EMI shields and stealth systems. To assess consistency, Shielding Effectiveness (*ShEff*) calculation includes components such as absorption ($ShEff_A$), reflection ($ShEff_R$), and multiple reflections ($ShEff_{MR}$). *ShEff* quantifies a shield's ability to attenuate EM signals, crucial for preventing EM interference. These *ShEff*components can be computed using the subsequent equations (10), (11), (12), and (13) [35]:

$$ShEff = ShEff_A + ShEff_R + ShEff_{MR} \tag{10}$$

$$ShEff_A = -10 \times \log_{10} \frac{TX}{1 - Ref} \tag{11}$$

$$ShEff_R = -10 \times \log_{10} \frac{1}{Ref} \tag{12}$$

$$ShEff_{MR} = -10 \times \log_{10} \left(1 - Ref^2\right) \tag{13}$$

where *TX* and *Ref* are transmission and reflection coefficients. The computations were conducted, and graphs illustrating the $ShEff_A$, and $ShEff_R$ are presented in Fig. 9. The $ShEff_A$ value remains consistently above 30 dB within the operational bandwidth and can be further enhanced with increased reflector thickness. A practical $ShEff_A$ requirement of over 10 dB ensures minimal impact from multiple reflections. Moreover, the $ShEff_R$ effect remains marginal, staying within 1 dB, indicating that the absorber design effectively contains incoming EM wave power. Notably, the suggested absorber configuration offers a non-metallic structure with an expansive absorption spectrum. Its ultra-slim profile marks it ideal for applications in Insulating and enclosing. Additionally, the absorber provides excellent absorption across a broad range of incident angles, enhancing its versatility.

VIII. COMPARISON AND FABRICATION OF PROPOSED ABSORBER

The proposed absorber is compared with relevant research articles, as shown in Table 1. It demonstrates a notable absorption bandwidth of 7.554 THz, accompanied by a compact design. Additionally, the absorber exhibits non-metallic properties and the capability to switch between insulating and metallic phases. Moreover, tunability is achieved by adjusting the properties of graphene and VO_2. Furthermore, owing to the symmetric design, the broadband

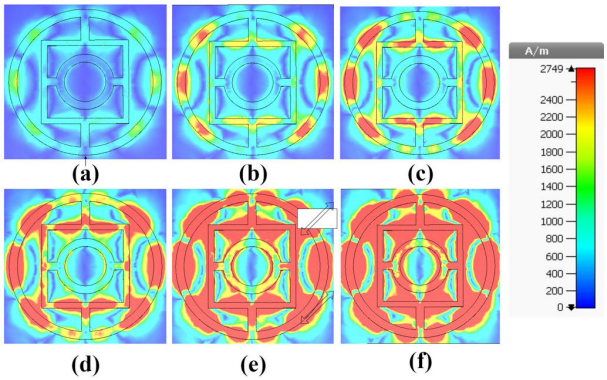

FIGURE 7. HF distribution on the proposed absorber at a frequency of 4.97 THz for different values of conductivity (σ_{VO_2}) in S/m.
(a) $\sigma_{VO_2} = 1\times10^2$, (b) $\sigma_{VO_2} = 1\times10^3$, (c) $\sigma_{VO_2} = 1\times10^4$, (d) $\sigma_{VO_2} = 1\times10^5$, (e) $\sigma_{VO_2} = 3\times10^5$, (f) $\sigma_{VO_2} = 5\times10^5$.

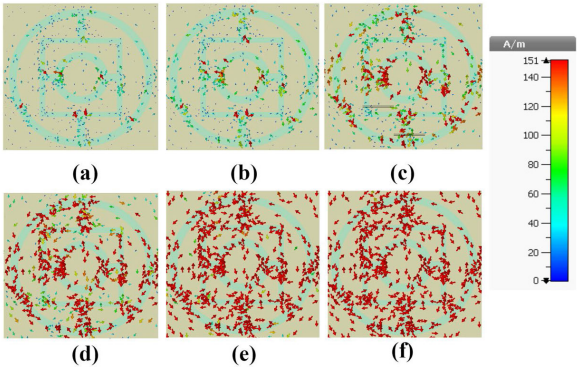

FIGURE 8. SC distribution on the proposed absorber at a frequency of 4.97 THz for different values of conductivity (σ_{VO_2}) in S/m.
(a) $\sigma_{VO_2} = 1\times10^2$, (b) $\sigma_{VO_2} = 1\times10^3$, (c) $\sigma_{VO_2} = 1\times10^4$, (d) $\sigma_{VO_2} = 1\times10^5$, (e) $\sigma_{VO_2} = 3\times10^5$, (f) $\sigma_{VO_2} = 5\times10^5$.

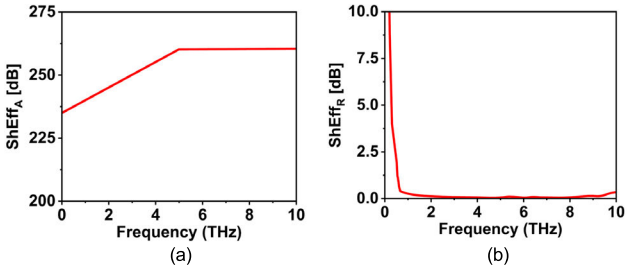

FIGURE 9. Frequency response of (a) ShEff$_A$, (b) ShEff$_R$.

absorber is insensitive to polarization and performs well at high incidence angles. The fabrication process of the suggested absorber for THz frequency applications involves a series of intricate steps, each contributing to its functionality and performance. Initially, the SiO_2substrate, characterized by a relative permittivity (ε_s) of 2.2, is prepared using standard fabrication techniques. The periodic pattern and unit cell configuration are then defined, typically using lithography, to ensure precise interaction of incident EM waves with the absorber. Following substrate preparation,

TABLE 1. Comparison analysis.

Ref	Material	t	f	BW	θ	S	T
[20]	VO_2/M	7.45	3.35 to 8.45	5.1	30°	Yes	Yes
[21]	ECCOSORB /M	920	0.1–16	15.9	70°	No	No
[22]	VO_2/M	10.66	2.30–8.65	6.35	50°	Yes	Yes
[23]	VO_2/M	8.2	3.01-6.79	3.78	45°	Yes	Yes
[24]	VO_2/M	22.34	6.6-8.9	2.3	60°	No	Yes
[25]	VO_2/M	7.4	3.01-7.27	4.26	55°	Yes	Yes
[14]	Graphene/ VO_2/M	21.9	1.31-3.18 and 4.45-8.40	1.87 and 3.95	60°	Yes	Yes
[26]	Graphene / VO_2/M	25.04	0-0.84 and 3.4-4.64	0.84 and 1.24	60°	Yes	Yes
This	**Graphene/ VO_2/ Non-Metallic**	**0.635**	**1.198-8.752**	**7.554**	**75°**	**Yes**	**Yes**

M: Metamaterial, t: Thickness (μm), f: Frequency (THz), BW: Bandwidth (THz), S: Switching, T: Tunable.

chemical vapor deposition (CVD) techniques are employed to grow a graphene layer atop the SiO_2 substrate. This graphene layer, serves as a crucial component in the absorber structure, offering exceptional conductivity and optical properties. To construct the resonating VO_2 layer, stencil deposition techniques are utilized, allowing for the precise positioning of three rings made of VO_2 on the graphene layer. VO_2, a compound known for its phase transition behavior at specific critical temperatures, plays a pivotal role in achieving dynamic absorption control within the absorber.

During the fabrication procedure, stringent quality control methods are applied to confirm the accuracy and integrity of each component. To effectively control the temperature of VO_2 in experiments, several methods can be employed. One common approach is to utilize external heating or cooling systems, such as resistive heaters or Peltier devices, to precisely regulate the temperature of the VO_2 sample. By carefully adjusting the temperature using these external systems, researchers can induce and control the phase transition of VO_2 with high accuracy. Additionally, advanced experimental setups may incorporate temperature sensors and feedback control mechanisms to monitor and maintain the desired temperature of the VO_2 sample throughout the experiment. This ensures stable conditions for studying the phase change behavior and its practical implications [36], [37], [38], [39], [40]. Also, advanced characterization techniques, such as scanning electron microscopy (SEM) and atomic force microscopy (AFM), are often employed to assess the structural integrity and performance of the fabricated absorber, validating its suitability for THz frequency applications.

IX. CONCLUSION

In conclusion, this paper introduces a pioneering ultrathin absorber that represents a significant advancement in THz technology. By leveraging the unique properties of VO_2 and graphene, we have achieved a non-metallic solution for wideband absorption, addressing a crucial need in the field. The remarkable tunable and switchable performance of our absorber marks a notable milestone in achieving frequency tunability across broadband absorption ranges. Moreover, its exceptional absorption characteristics, even at high incidence angles, underscore its potential for practical applications. Additionally, the absorber's contribution to enhancing Shielding Effectiveness in EMI shields and stealth systems further enhances its utility and value. Overall, our work lays a solid foundation for future developments in THz absorber technology and opens up exciting possibilities for advancements in various fields.

REFERENCES

[1] P. H. Siegel, "Terahertz technology," *IEEE Trans. Microw. Theory Techn.*, vol. 50, no. 3, pp. 910–928, Mar. 2002, doi: 10.1109/22.989974.

[2] H.-J. Song and T. Nagatsuma, "Present and future of terahertz communications," *IEEE Trans. THz Sci. Technol.*, vol. 1, no. 1, pp. 256–263, Sep. 2011, doi: 10.1109/TTHZ.2011.2159552.

[3] P. Upender and A. Kumar, "Implementing reconfigurable circularly polarized two port MIMO DRA for THz applications," *Opt. Quantum Electron.*, vol. 55, no. 10, pp. 1–23, Oct. 2023, doi: 10.1007/s11082-023-05188-8.

[4] P. Upender and A. Kumar, "Ultrathin, ultra narrow band DMMA for biosensing applications," *IEEE Trans. Nanobiosci.*, vol. 22, no. 3, pp. 529–537, Jul. 2023, doi: 10.1109/TNB.2022.3217077.

[5] P. Upender and A. Kumar, "Highly sensitive tunable dual-band THz refractive-based metamaterial sensor for biosensing applications," *IEEE Trans. Plasma Sci.*, vol. 51, no. 10, pp. 3258–3264, Oct. 2023, doi: 10.1109/TPS.2023.3314536.

[6] Y. Huang, Y. Shen, and J. Wang, "From terahertz imaging to terahertz wireless communications," *Engineering*, vol. 22, pp. 106–124, Mar. 2023, doi: 10.1016/j.eng.2022.06.023.

[7] K. Li and J. Yu, "Photonics-aided terahertz-wave wireless communication," *J. Lightw. Technol.*, vol. 40, no. 13, pp. 4186–4195, Jul. 2022, doi: 10.1109/JLT.2022.3161878.

[8] J. Zhang, N. Mu, L. Liu, J. Xie, H. Feng, J. Yao, T. Chen, and W. Zhu, "Highly sensitive detection of malignant glioma cells using metamaterial-inspired THz biosensor based on electromagnetically induced transparency," *Biosensors Bioelectron.*, vol. 185, Aug. 2021, Art. no. 113241, doi: 10.1016/j.bios.2021.113241.

[9] G. Varshney and P. Giri, "Bipolar charge trapping for absorption enhancement in a graphene-based ultrathin dual-band terahertz biosensor," *Nanosc. Adv.*, vol. 3, no. 20, pp. 5813–5822, Oct. 2021, doi: 10.1039/d1na00388g.

[10] P. Upender, S. P. Bharathi, K. Kumba, and A. Kumar, "A compact metamaterial biosensor for multi-virus detection with tunability and high incidence angle absorption," *IEEE Access*, vol. 11, pp. 131915–131925, 2023, doi: 10.1109/ACCESS.2023.3336815.

[11] S. Barzegar-Parizi, "Graphene-based tunable dual-band absorbers by ribbon/disk array," *Opt. Quantum. Electron.*, vol. 51, no. 6, pp. 1–11, Jun. 2019, doi: 10.1007/S11082-019-1882-0.

[12] N. Kiani, F. T. Hamedani, and P. Rezaei, "Switchable circular polarization in flower-shaped reconfigurable graphene-based THz microstrip patch antenna," *Anal. Integr. Circuits Signal Process.*, vol. 118, no. 2, pp. 259–270, Dec. 2023, doi: 10.1007/s10470-023-02215-2.

[13] Y. Ren and B. Tang, "Switchable multi-functional VO2-integrated metamaterial devices in the terahertz region," *J. Lightw. Technol.*, vol. 39, no. 18, pp. 5864–5868, Sep. 2021, doi: 10.1109/JLT.2021.3092952.

[14] B. Wu, X. Liu, G. Fu, G. Liu, Z. Liu, and J. Chen, "Bi-channel switchable broadband terahertz metamaterial absorber," *IEEE Photon. Technol. Lett.*, vol. 35, no. 1, pp. 15–18, Jan. 2023, doi: 10.1109/LPT.2022.3218133.

[15] A. Kumar and G. Varshney, "Thermally-electrically tunable broadband ultrathin metal-free THz absorber," *IEEE Photon. Technol. Lett.*, vol. 35, no. 22, pp. 1235–1238, Nov. 2023, doi: 10.1109/LPT.2023.3313935.

[16] G. Wang, T. Wu, J. Jiang, Y. Jia, Y. Gao, and Y. Gao, "Switchable terahertz absorber from single broadband to triple-narrowband," *Diamond Rel. Mater.*, vol. 130, Dec. 2022, Art. no. 109460, doi: 10.1016/j.diamond.2022.109460.

[17] P. Upender and A. Kumar, "Graphene-based ultra-wideband absorber for terahertz applications using hexagonal split ring resonators," *Phys. Scripta*, vol. 97, no. 6, May 2022, Art. no. 065503, doi: 10.1088/1402-4896/ac6af1.

[18] P. Upender and A. Kumar, "Design of a multiband graphene-based absorber for terahertz applications using different geometric shapes," *J. Opt. Soc. Amer. B, Opt. Phys.*, vol. 39, no. 1, p. 188, Jan. 2022, doi: 10.1364/josab.440757.

[19] X. Xu, R. Xu, and Y.-S. Lin, "A voltage-controllable VO_2 based metamaterial perfect absorber for CO_2 gas sensing application," *Nanoscale*, vol. 14, no. 7, pp. 2722–2728, Feb. 2022, doi: 10.1039/d1nr07746e.

[20] M. Rashki and M. R. Rakhshani, "An active broadband perfect absorber metamaterial based on hexagonal-patterned vanadium dioxide," *Plasmonics*, vol. 18, no. 4, pp. 1351–1359, Aug. 2023, doi: 10.1007/s11468-023-01846-5.

[21] Y. Zou, H. Lin, Y. Wu, H. Zhu, X. Zhang, and B.-X. Wang, "Theoretical investigation of an ultra-wideband tunable metamaterial absorber based on four identical vanadium dioxide resonators in the terahertz band," *J. Electron. Mater.*, vol. 52, no. 4, pp. 2852–2864, Apr. 2023, doi: 10.1007/s11664-023-10250-y.

[22] L. Zheng, R. Feng, H. Shi, and X. Li, "Tunable broadband terahertz metamaterial absorber based on vanadium dioxide and graphene," *Micromachines*, vol. 14, no. 9, p. 1715, Aug. 2023, doi: 10.3390/MI14091715.

[23] G. Yang, F. Yan, X. Du, T. Li, W. Wang, Y. Lv, H. Zhou, and Y. Hou, "Tunable broadband terahertz metamaterial absorber based on vanadium dioxide," *AIP Adv.*, vol. 12, no. 4, p. 45219, Apr. 2022, doi: 10.1063/5.0082295.

[24] Y. Zhang, P. Wu, Z. Zhou, X. Chen, Z. Yi, J. Zhu, T. Zhang, and H. Jile, "Study on temperature adjustable terahertz metamaterial absorber based on vanadium dioxide," *IEEE Access*, vol. 8, pp. 85154–85161, 2020, doi: 10.1109/ACCESS.2020.2992700.

[25] X. Wang, G. Wu, Y. Wang, and J. Liu, "Terahertz broadband adjustable absorber based on VO_2 multiple ring structure," *Appl. Sci.*, vol. 13, no. 1, p. 252, Dec. 2022, doi: 10.3390/app13010252.

[26] Q. Z. Wang, S. Y. Liu, G. J. Ren, H. W. Zhang, S. C. Liu, and J. Q. Yao, "Multi-parameter tunable terahertz absorber based on graphene and vanadium dioxide," *Opt. Commun.*, vol. 494, Sep. 2021, Art. no. 127050, doi: 10.1016/j.optcom.2021.127050.

[27] X. Li, W. Cai, J. An, S. Kim, J. Nah, D. Yang, R. Piner, A. Velamakanni, I. Jung, E. Tutuc, S. K. Banerjee, L. Colombo, and R. S. Ruoff, "Large-area synthesis of high-quality and uniform graphene films on copper foils," *Science*, vol. 324, no. 5932, pp. 1312–1314, Jun. 2009, doi: 10.1126/science.1171245.

[28] G. W. Hanson, "Dyadic Green's functions and guided surface waves for a surface conductivity model of graphene," *J. Appl. Phys.*, vol. 103, no. 6, Mar. 2008, Art. no. 064302, doi: 10.1063/1.2891452.

[29] R. Gupta, G. Varshney, and R. S. Yaduvanshi, "Tunable terahertz circularly polarized dielectric resonator antenna," *Optik*, vol. 239, Aug. 2021, Art. no. 166800, doi: 10.1016/j.ijleo.2021.166800.

[30] M. F. Ali, R. Bhattacharya, and G. Varshney, "Graphene-based tunable terahertz self-diplexing/MIMO-STAR antenna with pattern diversity," *Nano Commun. Netw.*, vol. 30, Dec. 2021, Art. no. 100378, doi: 10.1016/j.nancom.2021.100378.

[31] G. W. Hanson, "Dyadic Green's functions for an anisotropic, non-local model of biased graphene," *IEEE Trans. Antennas Propag.*, vol. 56, no. 3, pp. 747–757, Mar. 2008, doi: 10.1109/TAP.2008.917005.

[32] H. Jiang, Y. Wang, Z. Cui, X. Zhang, Y. Zhu, and K. Zhang, "Vanadium dioxide-based terahertz metamaterial devices switchable between transmission and absorption," *Micromachines*, vol. 13, no. 5, p. 715, Apr. 2022, doi: 10.3390/mi13050715.

[33] H. Liu, Z.-H. Wang, L. Li, Y.-X. Fan, and Z.-Y. Tao, "Vanadium dioxide-assisted broadband tunable terahertz metamaterial absorber," *Sci. Rep.*, vol. 9, no. 1, pp. 1–10, Apr. 2019, doi: 10.1038/s41598-019-42293-9.

[34] S.-A. Imam, K. M. Ishtiak, and Q. D. M. Khosru, "Graphene-VO_2-based-defect-induced tunable multiple narrowband unidirectional photonic terahertz absorber," *Opt. Mater. Exp.*, vol. 12, no. 7, p. 2653, Jul. 2022, doi: 10.1364/ome.462860.

[35] S. Celozzi, R. Araneo, P. Burghignoli, and G. Lovat, *Electromagnetic Shielding: Theory and Applications*. Piscataway, NJ, USA: IEEE Press, 2008.
[36] C. Song, J. Wang, B. Zhang, Z. Qu, H. Jing, J. Kang, J. Hao, and J. Duan, "Dual-band/ultra-broadband switchable terahertz metamaterial absorber based on vanadium dioxide and graphene," *Opt. Commun.*, vol. 530, Mar. 2023, Art. no. 129027, doi: 10.1016/j.optcom.2022.129027.
[37] S. Barzegar-Parizi, A. Ebrahimi, and K. Ghorbani, "Terahertz wideband modulator devices using phase change material switchable frequency selective surfaces," *Phys. Scripta*, vol. 98, no. 6, May 2023, Art. no. 065531, doi: 10.1088/1402-4896/acd6c7.
[38] Y. Qi, Y. Wen, H. Chen, and X. Wang, "Dynamically tunable terahertz quadruple-function absorber based on a hybrid configuration of graphene and vanadium dioxide," *Nanotechnology*, vol. 35, no. 9, Dec. 2023, Art. no. 095202, doi: 10.1088/1361-6528/ad0c76.
[39] N. Mou, B. Tang, J. Li, H. Dong, and L. Zhang, "Switchable ultra-broadband terahertz wave absorption with VO2-based metasurface," *Sci. Rep.*, vol. 12, no. 1, pp. 1–8, Feb. 2022, doi: 10.1038/s41598-022-04772-4.
[40] S. Barzegar-Parizi, A. Ebrahimi, and K. Ghorbani, "Two bits dual-band switchable terahertz absorber enabled by composite graphene and vanadium dioxide metamaterials," *Sci. Rep.*, vol. 14, no. 1, pp. 1–14, Mar. 2024, doi: 10.1038/s41598-024-56349-y.

PATRI UPENDER received the B.Tech. degree in electronics and communication engineering from JNTU Hyderabad, in 2008, the M.Tech. degree in RF and microwave from the Indian Institute of Technology Roorkee, in 2010, and the Ph.D. degree from the National Institute of Technology Warangal, in 2023. He is currently an Assistant Professor with the School of Electronics Engineering, Vellore Institute of Technology, Chennai, Tamil Nadu, India. He has about 12 years of research experience in the development of antennas and metamaterials. He has more than 35 publications in various journals and conferences at national and international level. His research interests include biosensing applications, metamaterials, dielectric resonator antennas, microwave, millimeter wave antennas, radar engineering, THz, 6G devices, RF communication, and graphene devices.

P. A. HARSHA VARDHINI (Senior Member, IEEE) received the bachelor's degree in ECE from JNTUH, in 2001, the master's degree in ECE from GVM, in 2005, and the Ph.D. degree in VLSI design from the Department of ECE, JNTUH, in 2015. She is the Dean IQAC and the Head of the Department of Electronics and Communication Engineering, Vignan Institute of Technology and Science, Hyderabad, Telangana. She has 21 years of teaching and research experience. She is the author of over 116 publications in various journals and conferences at national and international level, including SCI, Scopus, IEEE, Springer, Elsevier, and UGC. She holds three patents and nine books/book chapters. Her research interests include VLSI, FPGA architectures, the Internet of Things, artificial intelligence, and machine learning. She was a recipient of various awards and accolades, such as the NPTEL STAR Awards, the Best Paper Awards, the Best Teacher Award, and the Women Researcher Award. She serves as a Secretary for IEEE WIE AG Hyderabad Section. She has organized and chaired sessions at various prestigious IEEE and Springer conferences. She is an editorial board member and a reviewer of renowned international journals and conferences.

KRISHNA KUMBA received the B.Tech. degree in electrical and electronics engineering from JNTU Hyderabad, India, in 2008, the M.Tech. degree in control system from the National Institute of Technology Kurukshetra, Haryana, India, in 2010, and the Ph.D. degree from the National Institute of Technology (NIT) Tiruchirappalli, India, in 2023. He is currently an Assistant Professor with the School of Electrical Engineering, Vellore Institute of Technology, Chennai, Tamil Nadu, India. His research interests include power system planning and reliability, solar photovoltaics, renewable energy systems, solar tracking systems, battery management systems, machine learning, and optimization.

S. PRASANNA BHARATHI received the B.Tech. degree in electronics and communication engineering from the SSN College of Engineering affiliated to University of Madras, the master's degree in microelectronics from Victoria University, Melbourne, Australia, and the Ph.D. degree in remote sensing from the Saveetha School of Engineering, SIMATS. Currently, he is an Assistant Professor with Vellore Institute of Technology, Chennai. He has around 14 years of teaching experience and four years of industry experience. He has published around 25 papers in various reputed international journals, national and international conferences. His research interests include remote sensing, VLSI design, and the IoT. He is an Active Member of the Institution of Engineering and Technology (IET). He holds the position of the Chairperson of IET Chennai Local Network and Treasurer in IET Communities Committee of South Asia.

AMARJIT KUMAR (Senior Member, IEEE) received the M.Tech. and Ph.D. degrees from the Indian Institute of Technology Roorkee, India, in 2012 and 2018, respectively. He has about ten years of research work experience in the development of passive and active RF circuits with concurrent multiband, reconfigurable, and multifunctional capabilities for next-generation wireless applications; and the development of RF/microwave sensors for the wireless monitoring of pressure and temperature variations for the Industrial Internet of Things applications. He has designed, fabricated, and characterized reflection type microwave phase shifter, dual band tunable bandpass filters, Wilkinson power dividers, branch-line couplers, planar antennas, reconfigurable filtering dual band low-noise amplifiers, voltage-controlled oscillator, and wireless sensors using RF transceivers. He has published more than 40 research papers, one Indian patent, and three book chapters in reputed international journals and conferences. He served as the Chairperson for IEEE MTT Society SBC IIT Roorkee, from October 2013 to April 2018. Currently, he is associated with NIT Warangal as an Assistant Professor with the ECE Department. His current research focus is in design of millimeter-wave and terahertz (THz) devices and biosensors for B5G and future 6G wireless communication systems. He is serving as the present Vice Chair for the IEEE Photonics Society Chapter of Hyderabad Section, India. He has served as a reviewer for some of the reputed IEEE journals, letters, and transactions; and also served as a TPC member, the technical track chair, and the session chair for a number of IEEE conferences.